



Microstructure characterization of dissimilar metal welds of innovative high- and medium-entropy alloys to austenitic stainless steels joint by tungsten inert gas and friction stir welding

Tim Richter¹ · Kjell Erxleben¹ · Michael Rhode^{1,2} · Dirk Schroeppfer¹ · Thomas Michael¹ · Andreas Boerner¹

Received: 10 March 2023 / Accepted: 23 October 2023 / Published online: 28 December 2023
© International Institute of Welding 2023

Abstract

The new multi-element alloying concept of systems with defined entropy (HEA — high-entropy alloy or MEA — medium-entropy alloy) is increasing in material research interest. Improved properties or combinations of properties are shown by several systems. Thus, the resulting microstructures and production of HEA/MEA as well as properties have been primarily investigated so far. Furthermore, processing is a key issue to transfer HEA/MEA systems to real components. Since welding is the most important joining process for metals, it is crucial to investigate the influence of welding to guarantee component integrity. Since most HEA are made of expensive alloying elements such as Co or Ni, they will not be used entirely as structural materials. Thus, it can be advantageous to weld conventional alloys such as austenitic stainless steels with the HEA and MEA to produce components that are both application-oriented and economically viable. Therefore, in this paper, first results of dissimilar metal welding, by tungsten inert gas (TIG) and friction stir welding (FSW), of a CoCrFeMnNi HEA as well as a CoCrNi MEA with a conventional AISI 304 austenitic stainless steel are presented. The focus is on the microstructure formation due to the two welding processes. The results of TIG welding show a dendritic microstructure, whereas in FSW both materials are stirred but still coexist.

Keywords DMW · TIG · FSW

1 Introduction

Since the first publications in 2004 [1, 2], material research interest in high- and medium-entropy alloys (HEA and MEA) has steadily increased as a single-phase class of multiple principal element alloys (MPEA). These novel materials contain at least five (HEA) or three (MEA) alloying elements with possible concentrations between 5 and 35 at.% for each element and are defined as single-phase solid solutions. This distinguishes the HEA concept from conventional alloys with one or two main alloying elements, as used in

steel or Al alloys. These novel alloy concepts offer enormous potential for the substitution of conventional alloys due to excellent property combinations, e.g., to overcome the traditional trade-off between strength and ductility [3, 4] or to achieve high strength combined with excellent corrosion resistance, even outperforming Ni alloys in high-temperature applications [5]. In the case of more than one phase, the term CCA (Complex Concentrated Alloys) has become established for these materials. To enable the use of HEA as functional or structural materials in real components, economic and safe processability is important in addition to the desired special application properties.

The focus of this research study is therefore on welding as the primary joining process for metals. Most scientific work is devoted to the so-called “Cantor” alloy ($\text{Co}_{20}\text{Cr}_{20}\text{Fe}_{20}\text{Mn}_{20}\text{Ni}_{20}$, named after inventor Brian Cantor) [1]. Despite the many alloying elements, the material exhibits a single-phase, face-centered cubic (fcc) microstructure. This quinary alloy (HEA) as well as the ternary alloy $\text{Co}_{33.3}\text{Cr}_{33.3}\text{Ni}_{33.3}$ (MEA) exhibit excellent mechanical properties, e.g., under cryogenic conditions [6] and corresponding low-temperature

Recommended for publication by Commission II—Arc Welding and Filler Metals

✉ Tim Richter
tim.richter@bam.de

¹ Department 9. Komponentensicherheit, Bundesanstalt Für Materialforschung Und -Prüfung (BAM), Berlin, Germany

² Institut Für Werkstoff- Und Fügetechnik IWF, Otto-Von-Guericke Universität, Magdeburg, Germany

components. Previous studies on the weldability of HEAs have increasingly focused on solid-state friction stir welding (FSW) [7, 8], TIG [9], electron beam, and laser beam fusion welding [5, 10]. Weldability as a material property (according to ISO/TR 581:2005 [11]) is the ability to produce a component from a given material by welding if it can perform the intended tasks over its service life under the given manufacturing conditions (technological process) and taking into account the design. Against this background, previous investigations have shown good quality weldability for CoCrFeMnNi HEA. This is mainly since further process steps, such as preheating or post-weld heat treatment processes, can be dispensed with [5, 12]. However, the practical welding processing of these HEA and MEA grades is still largely unexplored in terms of component-related specimen dimensions, since welding tests have generally been carried out on very small dimensioned specimens. In contrast to arc welding, such as TIG (melting of the substrate by the welding arc), in FSW the welding heat is generated by the friction of the rotating tool shoulder with the material to be welded. A significant advantage is the friction-induced process temperature, which is usually in the range of 75–90% of the melting point T_m [13]. At these temperatures, the material is in a highly viscous state and is stirred in the melt zone by a pin on the tool. This prevents the precipitation of intermetallic phases in the weld metal (WM) and thus the tendency to brittle fracture. So-called welding defects, such as flaws in the weld seam or deviations from the nominal geometry, are referred to as “defects” according to specifications in DIN EN ISO 6520–2 [14].

Since most HEA are made of expensive alloying elements such as Co or Ni, they will not be used entirely as structural materials. Thus, it can be advantageous to weld conventional alloys such as austenitic stainless steels with the HEA and MEA to produce components that are both application-oriented and economically viable. Currently, the number of research studies on HEA-steel DMWs is rare so far. For example, Oliveira et al. [15, 16] studied a laser-welded DMW of CoCrFeMnNi to AISI 316L, and Samiuddin et al. [17] studied the diffusion welding behavior of CoCrNi MEA and AISI304 DMW. Therefore, in this paper, first results of dissimilar metal welding, by tungsten inert gas (TIG) and friction stir welding (FSW), of a CoCrFeMnNi HEA as well as a CoCrNi MEA with a conventional AISI 304 austenitic stainless steel are presented. The focus is on the microstructure formation due to the two welding processes. The results of TIG welding show a dendritic microstructure, whereas in FSW both materials are stirred but still coexist.

2 Experimental

2.1 Material production

The production of both alloys was carried out by melting pure elements (purity: 99.9 wt.%) with a vacuum induction

Table 1 Chemical composition in atomic % of CoCrFeMnNi HEA and CoCrNi MEA by EMPA and AISI 304 by OES analysis (for AISI 304 only the main alloying elements are specified)

	Co	Cr	Fe	Mn	Ni
HEA	19.7	20.7	19.6	20.1	19.9
MEA	33.0	34.3	-	-	32.7
AISI 304	-	20.4	70.2	1.6	7.8

furnace and homogenization at 1200 °C for 48 h. Material production is given in more detail in [6]. The ingots with a diameter of 40 mm were cold-rolled to a thickness of 1.2 mm followed by recrystallization annealing at 1020 °C (HEA) or 1060 °C (MEA) for 60 min [18]. Afterward, a single-phase fcc alloy with some minor production-related impurities was present (Cr- and Mn-rich oxides) [19]. The chemical compositions of the alloys were determined by electron microprobe analysis (EMPA) and are given in Table 1. The plates were cut to a dimension of 75 × 20 mm², for the welding experiments.

The commercially available corrosion-resistant austenitic steel 304 using the AISI nomenclature (American Iron and Steel Institute) with 1.2-mm thickness is used in a hot-rolled condition. The chemical composition, measured by optical emission spectroscopy (OES), is given in Table 1.

2.2 Tungsten inert gas welding

The TIG welding experiments were carried out using a specially designed and custom manufactured specimen clamping system for the specimen dimensions and to realize a degree of stiffness or restraint as it appears in real welded joints. The test setup is shown in Fig. 1. In addition to the TIG torch, a gas trailing nozzle can be seen to cover the weld metal (WM) even after welding. The same applies to the root, which is to be protected from oxidation by means of shielding gas. A Polysoude PC 600 TIG system was used (pulsed arc mode), ensuring full penetrating weld seam with approximately 70-mm length. The welding parameters are shown in Table 2.

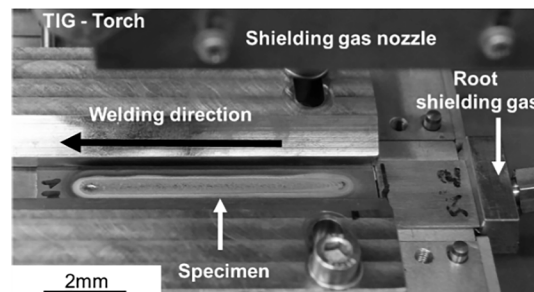


Fig. 1 Welding experiment setup for TIG welding

2.3 Friction stir welding process

Table 2 Welding parameters for TIG welding tests

Basic current	Peak current	Arc voltage	Shielding gas
35 A	90 A	10 V	I1-Ar
Pulse frequency	Welding speed	Heat input	Root shielding gas
4 Hz	300 mm/min	0.133 kJ/mm	R1-ArH-7.5

The FSW tests were carried out on a 5-axis machining center DMU 65 (DMG MORI). The movement of the tool was path-controlled. Figure 2 shows the test setup. The FSW tool consisted of a sintered W-alloy with 1.5 wt.% La_2O_3 . The tool shoulder (diameter: 8 mm) was concave. The tool pin was 1.05 mm long and tapered (diameter: 2.0 to 2.4 mm). In addition, three surfaces were machined on the pin to support the material transport. In the test, the tool was set at 2° against the feed direction. The plunge speed was $10 \text{ mm}\cdot\text{min}^{-1}$, the rotational speed 3000 min^{-1} , and the feed speed $100 \text{ mm}\cdot\text{min}^{-1}$ (see Table 3). Since during FSW processing, the specimen location (in terms of the material, which is on the retreating side/RS or at the advancing side/AS) can influence the weld results, the position of the AISI 304 was systematically varied at for both RS and AS. Thus, the AISI 304 is on the RS with the HEA and on the AS with the MEA.

2.4 Analysis

For the subsequent light optical microscopic (LOM) examination, cross sections of the weld seam were machined, ground, and finally polished with 1- μm diamond paste. The microstructure was etched using modified Bloech-Wedel-II ($\text{K}_2\text{S}_2\text{O}_5$ reduced by 2 g/L) etchant for 30 s at room temperature, respectively. To investigate the microstructure, the prepared cross sections were examined by LOM (Polyvar

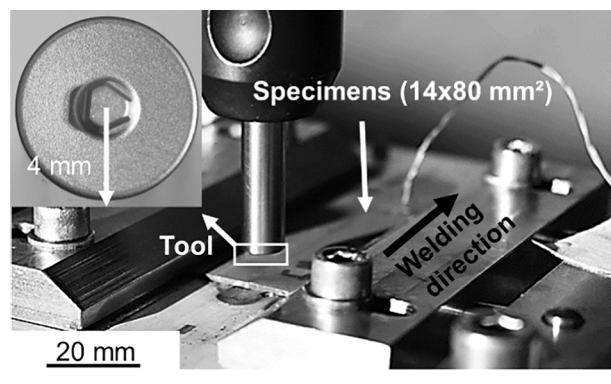


Fig. 2 Welding experiment setup for FSW

Table 3 Welding parameters for TIG welding tests

Rotation speed	Feed	Inclination angle
3000 1/min		$100 \text{ mm}\cdot\text{min}^{-2^\circ}$
Test implementation		Welding speed
Position controlled		300 mm/min

Met from Reichert-Jung, Germany) and scanning electron microscopy (SEM; Phenom XL from Thermo Fisher Scientific, Germany). The SEM was also used to perform the EDX analysis.

3 Results and discussion

3.1 Tungsten inert gas welding

In order to detect welding defects such as cracks or pores, the results of the radiographic test are shown in Fig. 3. Here it can be seen that no unacceptable imperfections such as cracks occur. Only at the joint between the MEA and the AISI 304 the seam fell through towards the end. The reason for this could be heat buildup in the material during welding, because these alloys have low thermal conductivity λ of HEA with $13.7 \text{ W}/(\text{m}\cdot\text{K})$ [20], MEA with $11.4 \text{ W}/(\text{m}\cdot\text{K})$ [20], and austenitic steel with $16.2 \text{ W}/(\text{m}\cdot\text{K})$ [21]. However, since this only affects a small part of the weld, the welding parameters used to be well suited for these material combinations. All other tests were performed on integral sections of the welds. Additionally, in both welds a dark area at the fusion line on the HEA/MEA side is noticeable. In that case, a higher dose of radiation can penetrate the specimen and exposes to the film. The reason could be a smaller

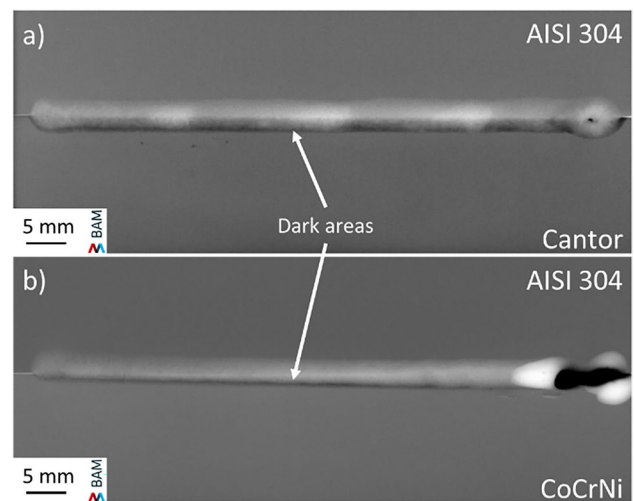


Fig. 3 X-ray radiographic inspection for the CoCrFeMnNi HEA (a) and CoCrNi MEA (b) TIG-welded joints with AISI 304

specimen thickness or a difference in local density (lower density allows more radiation to pass through). This will be discussed in the following sections.

Figure 4 shows the LOM images of the cross sections of the welded AISI 304 joints of the CoCrFeMnNi HEA (a) and the CoCrNi MEA (b). In both images, no weld imperfections can be seen; moreover, a full penetration weld is discernible, even though with an offset of the respective weld partners. In the case of the HEA joint, dendritic solidification is clearly visible in the WM. Moreover, an influence on the heat-affected zone (HAZ) is evident due to an increased susceptibility to etching compared to the base material (BM).

On the AISI 304 side, there is no clear influence on the HAZ compared to the BM with the low LOM magnification. However, due to the offset of the two welded plates, one edge of the AISI material protrudes into the WM. LOM analysis of the MEA/AISI 304 (Fig. 4(b)) joint shows a marked difference in the etching of the two materials, with the AISI 304 being significantly more susceptible to Bloech-Wedel-II etching. Due to the low susceptibility of the CoCrNi MEA to etching, no conclusions can be made about the weld metal and HAZ influence on the MEA side. Only a few darker spots can be seen in the WM, being not completely melted BM of the AISI 304. Regarding the mentioned dark areas in the radiographic results (Fig. 3), the offset visible in Fig. 4 may be caused by a slight decrease in plate thickness, which can be seen especially in the HEA/AISI 304 weld. However, the offset over the weld length was not as constant as the dark areas in the radiographic test, so this is ruled out as the main reason.

The results of SEM and EDX examinations of the HEA/AISI 304 TIG-welded joint are given in Fig. 5. The area around the fusion line is shown in Fig. 5(a), wherein no

microstructural change of the HAZ can be seen. Only an increased susceptibility to etching during specimen preparation around the fusion line can be seen by the strong pitting in this area. This is an indication of reduced corrosion resistance in certain media in the HAZ. The line scan over this area (Fig. 5(b)) shows that from the fusion line onwards the Fe content increases and the Mn, Ni, and Co contents in the WM decrease. Since Ni and Co with reduced contents have a greater density (both 8.9 g/cm^3 [22]) than Fe with increased content (7.87 g/cm^3 [22]), there should be a reduced density in this range, which explains the mentioned darker areas in the radiographic test (Fig. 3(a)).

In addition, Fig. 5(c) shows that Cr, Mn-rich oxides are present, which could be the reason for the pitting, as areas around these oxides could be Cr-depleted, resulting in reduced corrosion resistance, as in intergranular corrosion. However, Cr depletion cannot be confirmed by EDX line scan. In addition, the line scan shows an area of highly elevated Fe content. This should be steel material that has not been completely melted, due to the higher melting temperature of the steel ($\sim 1450 \text{ }^\circ\text{C}$ [21]) compared to the HEA ($1289 \text{ }^\circ\text{C}$ [23]). The EDX mapping of the WM in Fig. 5(d) shows a microstructure with segregations in which regions are enriched in Mn and the other regions are enriched in Fe. For Co, Cr, and Ni, no conclusion about local segregations can be clearly drawn from the results. This is similar to the studies of Wu et al. [24] for TIG welding of a CoCr-FeMnNi alloy, which found increased Mn contents in the interdendritic regions and increased Fe contents in the dendrite cores. However, Fig. 5(d) also shows a preferential dissolution of the interdendritic, i.e., Mn-rich, regions during etching, indicating that inhomogeneous corrosion properties are present in the WM. This is also supported by the fact that Yang et al. [25] show a degradation of the corrosion properties in an acid with increasing Mn content.

Figure 5(e) shows the area around the fusion line from the AISI 304 stainless steel to the WM. In that case, a dendritic microstructure can also be seen directed away from the fusion line. The EDX line scan (Fig. 5(f)) shows that the amount of Fe depletes from the fusion line inhomogeneous. In addition, the proportions of Co, Ni, and Mn increase. The Cr content, on the other hand, is constant over the entire measured range.

The SEM and EDX results of the TIG-welded joint made by AISI 304 with the CoCrNi MEA are shown in Fig. 6. The area around the fusion line on the side of the CoCrNi MEA shows in Fig. 6(a) no microstructural change in the HAZ compared to the recrystallized BM. In addition, an epitaxial and dendritic microstructure away from the fusion line can be seen in the WM. The EDX line scan over this area (Fig. 6(b)) reveals that there is no influence in the HAZ on the chemical composition. From the fusion line, the amount of Fe in the WM increases,

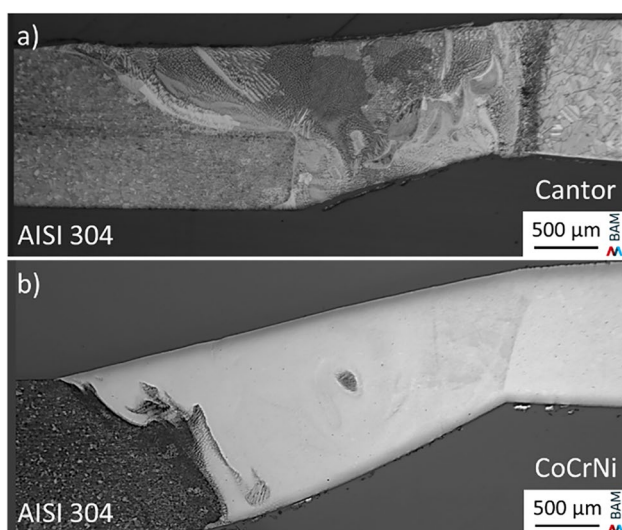


Fig. 4 LOM cross sections of the TIG-welded CoCrFeMnNi HEA (a) and the CoCrNi MEA (b) with AISI 304

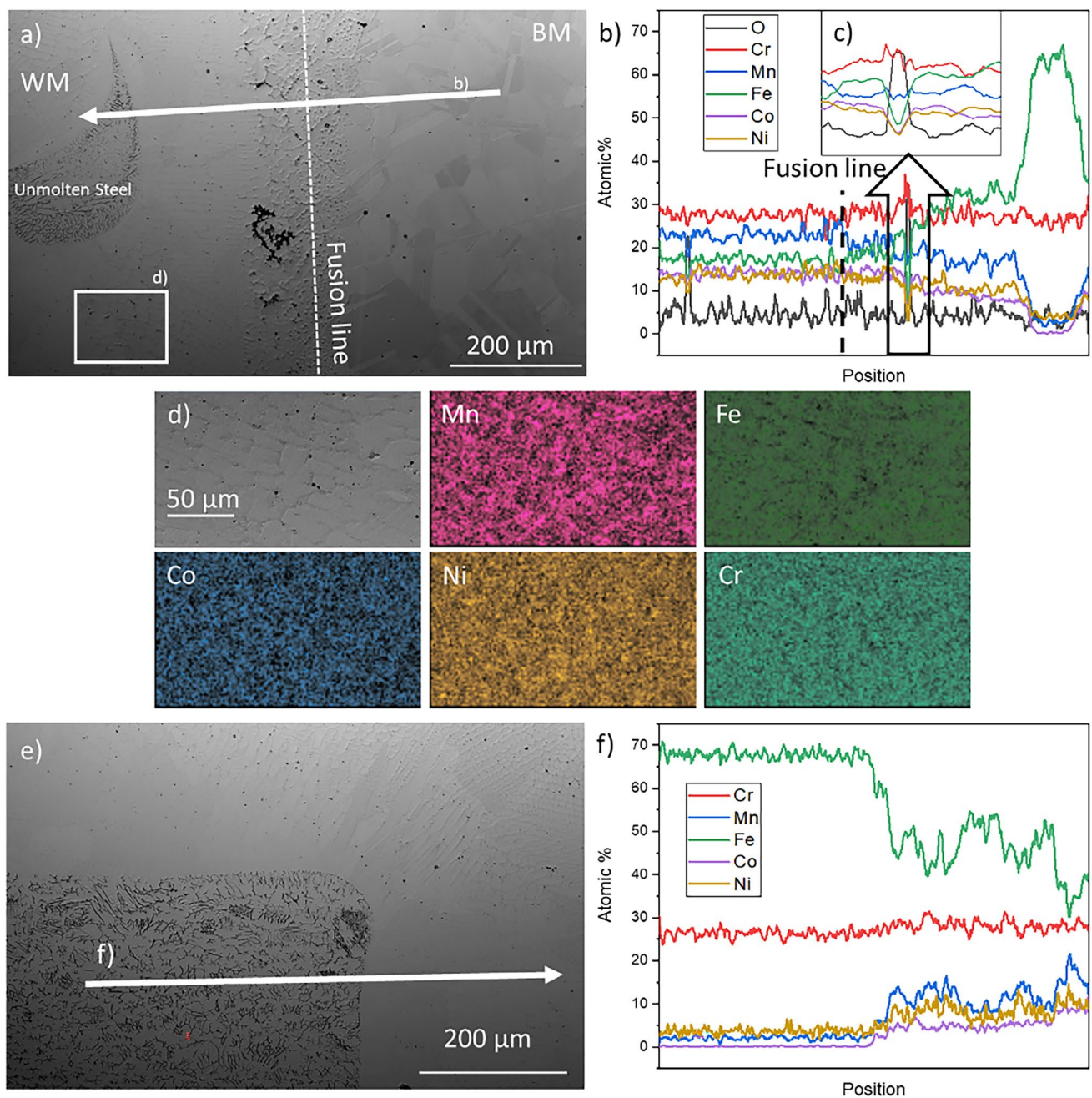


Fig. 5 SEM examinations of the HEA and AISI 304-welded joint: transition from HEA BM to WM (a) with EDX line scan (b, c) EDX mapping of WM (d) and transition from AISI 304 BM to WM (e) with EDX line scan (f)

even if irregularly. This, together with the reduced contents of Co and Ni, like the AISI 304/HEA weld, could lead to a locally reduced density compared to the MEA BM and explain the dark areas of the radiographic test (Fig. 3(b)). In addition, Cr-rich oxides in the HAZ can also be detected in the MEA, which originate from the material production. The EDX mapping of the WM shows a dendritic microstructure with interdendritic regions enriched in Co, Cr, and Ni. The dendritic core regions are rich in

Fe. During etching of the samples, the Fe-rich dendritic areas tend to dissolve, and therefore, these areas might show a reduced corrosion resistance, but of course this also depends on the medium. On the AISI 304 side, the area around the fusion line is shown in Fig. 6(d). In that case, the tempering processes in the HAZ show the dissolved directional microstructure from rolling. In addition, there is not molten steel material in the WM of this welded joint, although the melting temperature of the austenitic

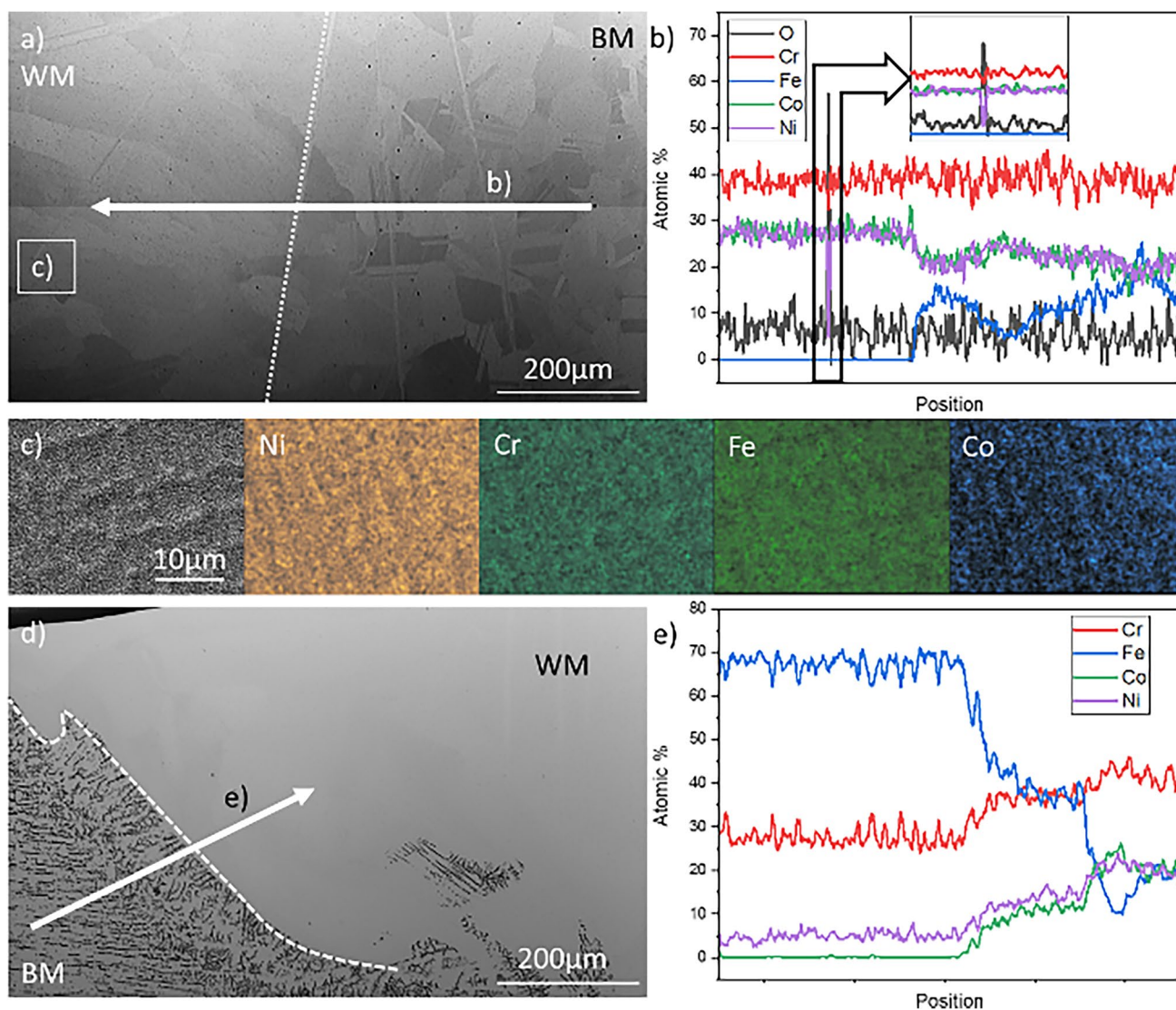


Fig. 6 SEM examinations of the MEA and AISI 304-welded joint: transition from MEA BM to WM (a) with EDX line scan (b), EDX mapping of WM (c), and transition from AISI 304 BM to WM (d) with EDX line scan (e)

steel (1450 °C [21]) is only slightly higher than that of the MEA (1417 °C [26]). The line scan over this area in Fig. 6(e) shows a strong and uneven reduction of the Fe content from the melt line towards the WM. On the other hand, the Co, Cr, and Ni contents increase in this area. As a result, Cr accounts for the largest fraction of the chemical composition of the WM.

3.2 Friction stir welding

Figure 7 shows the results of X-ray radiographic testing performed on the FSW-welded joints. Here a clear difference can be seen between the welds of the AISI 304 joined to the HEA (a) and the MEA (b). While the HEA has a clear defect running along the entire weld length slightly next to

the weld center on the HEA side, the MEA weld has no obvious defects. The reason for this may be, on the one hand, the greater difference in melting temperatures, related to a greater difference of the temperature-induced plasticizing behavior, between the HEA and AISI 304 compared to the MEA; on the other hand, the positioning of the plates could be a reason. Hence, the HEA with the lower melting temperature is on the AS and the steel with the higher melting temperature is on the RS. Which is the other way around for the MEA. Regardless, it can be stated that the welding process for the MEA/AISI 304 joint is well designed, whereas the process for the HEA/AISI 304 combination needs further adjustment.

The cross sections of the FSW joints are shown in Fig. 8. The HEA/AISI 304 combination (Fig. 8(a)) shows a tunnel

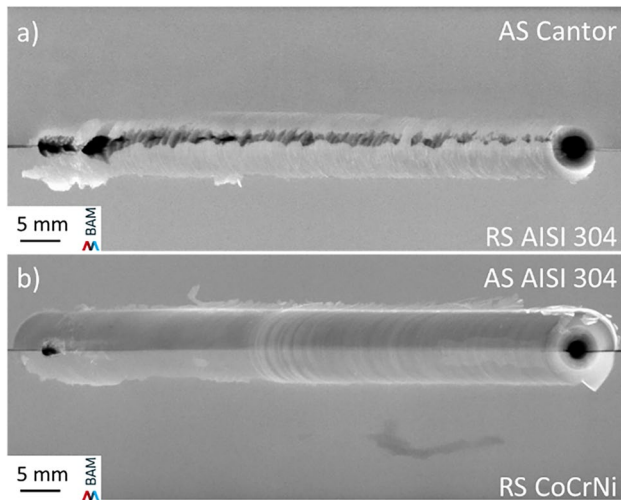


Fig. 7 X-ray radiographic inspection for the CoCrFeMnNi HEA (a) and CoCrNi MEA (b) TIG-welded joints with AISI 304

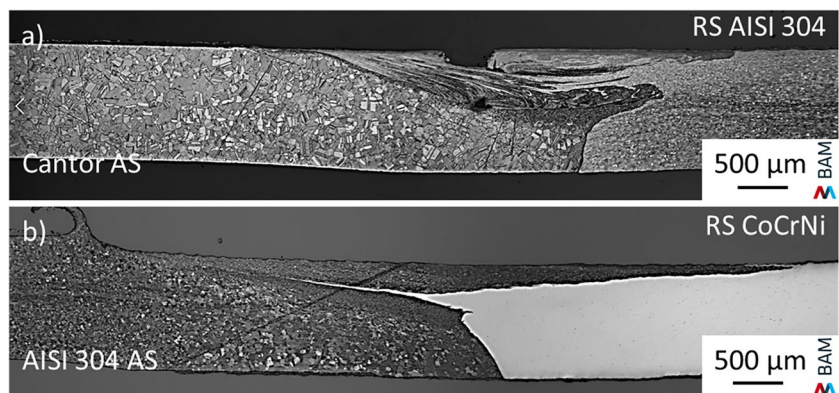
defect in the center of the plate, as already described in the radiographic test, and a pin-shaped impression on the surface. Furthermore, the weld was not completely penetrated, as a gap separates the two initial sheets on the root side. In the stir zone (SZ), a fine-grained lamellar mixing of the two materials can be seen, which will be explained in more detail later in this section. The combination of MEA and steel (Fig. 8(b)) clearly shows the difference in sample preparation of the two materials, as the brighter MEA is hardly susceptible to etching. This color difference also shows that the two materials have hardly been mixed and can be found both in the mixed SZ. Thus, darker fine-grained material can be seen on the surface, with the steel being stirred from the AS into the SZ. A light MEA line is clearly visible below the surface, thinning from the RS through the stirred zone. On the root side, the steel in the thermomechanical-affected

zone (TMAZ) shows a larger grain than in the base material, so that a recrystallization process can be assumed in this area.

The SEM and EDX examinations of the HEA/304 joint, shown in Fig. 9, indicate no effect on the TMAZ on the HEA side. However, the previously described tunnel defect is clearly visible at the transition of the stirred zone to the TMAZ. In addition, the EDX mapping in the top area clearly shows that both alloys are lamellar next to each other, since the Fe-rich areas hardly show any Co or Mn. In addition, the results show that W-particles are distributed throughout the SZ with an increased agglomeration at the transition of the SZ and the TMAZ. These W-particles are abrasive wear particles of the tool. It can be concluded that the process needs to be further adapted to obtain defect-free DMW with using the CoCrFeMnNi HEA and the AISI 304. It is recommended to first swap the sides of the material sheets in terms of the HEA to the RS and the steel from the AS.

Figure 10 shows the SEM and EDX results of the MEA/AISI 304 joint. Figure 10(a) shows how MEA material is drawn through the SZ. However, the line scan across this phase displaces a portion of Fe in this region, indicating that the materials are mixed in this region. In addition, a fine-grained microstructure with proportions of Co, Cr, Fe, and Ni can be seen above this surface area. This indicates that the materials are mixed. The situation is different in the TMAZ/stirring zone below this area, where the composition corresponds to that of steel AISI 304, i.e., any material mixing occurred. Compared to the fine-grained SZ, no grain refinement can be seen on the RS in the MEA material, so that a microstructure with coarse globular grains is still present. It can be noted that no defects were detected in the MEA/AISI 304 joint. This shows that the selected welding process is suitable for these joints. However, further investigations regarding the mechanical properties would have to follow to make conclusive statements.

Fig. 8 LOM cross sections of the FSW CoCrFeMnNi HEA (a) and the CoCrNi MEA (b) with AISI 304



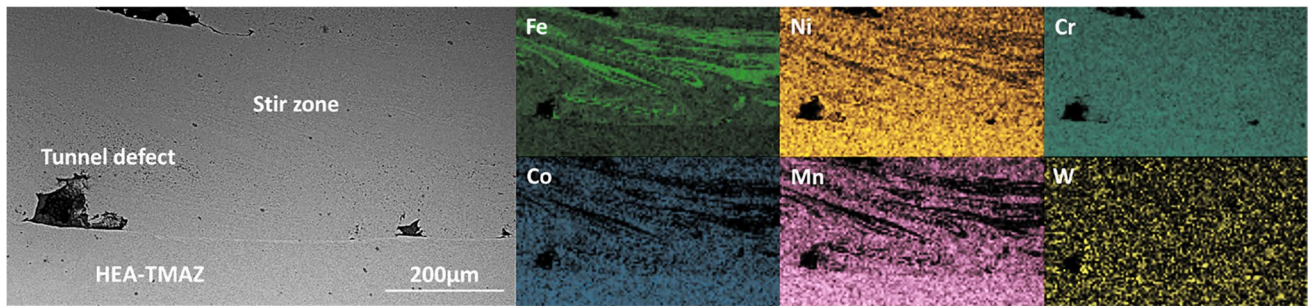
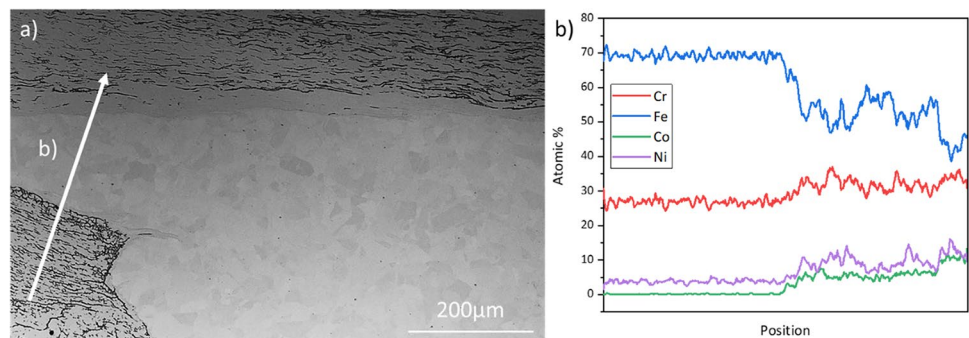


Fig. 9 SEM examinations of the HEA and AISI 304 FSW joint with EDX mapping

Fig. 10 SEM examinations of the MEA and AISI 304 FSW joint (a) with EDX-line scan (b)



4 Conclusions

The investigations of the DMW of HEA/MEA with the austenitic steel AISI 304 allow the following conclusions:

- A CoCrFeMnNi HEA and a CoCrNi HEA can be welded defect-free to a conventional austenitic steel using TIG welding.
- Both combinations show a dendritic microstructure with a gradient in chemical composition. In addition, not completely molten steel islands were detected in the WM. Whereby the influence of the very inhomogeneous microstructure on mechanical and corrosive properties needs further investigation.
- FSW showed a difference in the weld quality of the DMW of HEA and MEA with the austenitic steel compared to the TIG welds, as the HEA/304 combination exhibited a tunnel defect and incomplete penetration. Whether the reasons are due to the selected parameters, the larger difference in melting temperatures or the arrangement (alternation of AS and RS) needs further investigation.
- The MEA/AISI 304 combination showed no obvious weld imperfections and thus exhibited better weldability by using FSW with the selected welding parameters. The SZ shows a fine-grained microstructure with a chemical composition that suggests a mixture of materials.

Acknowledgements We would like to thank Prof. G. Laplanche and M. Schneider from the TU Bochum for providing the investigated materials, M. Grunwald for the irradiation tests, and M. Marten for the metallographic sample preparation.

Data availability The data are available by contacting the first author.

Declarations

Conflict of interest The authors declare no competing interests.

References

1. Cantor B, Chang ITH, Knight P, Vincent AJB (2004) Microstructural development in equiatomic multicomponent alloys. *Mater Sci Eng, A* 375–377:213–218
2. Yeh JW, Chen SK, Lin SJ, Gan JY, Chin TS, Shun TT, Tsau CH, Chang SY (2004) Nanostructured high-entropy alloys with multiple principal elements: novel alloy design concepts and outcomes. *Adv Eng Mater* 6(5):299–303
3. Manzoni AM, Glatzel U (2020) High-entropy alloys: balancing strength and ductility at room temperature, Reference Module in Materials Science and Materials Engineering
4. Miracle DB, Senkov ON (2017) A critical review of high entropy alloys and related concepts. *Acta Mater* 122:448–511
5. Rhode M, Richter T, Schropfer D, Manzoni AM, Schneider M, Laplanche G (2021) Welding of high-entropy alloys and compositionally complex alloys—an overview. *Welding in the World* 65(8):1645–1659
6. Laplanche G, Kostka A, Reinhart C, Hunfeld J, Eggeler G, George EP (2017) Reasons for the superior mechanical properties of

- medium-entropy CrCoNi compared to high-entropy CrMn-FeCoNi. *Acta Mater* 128:292–303
7. Park S, Nam H, Na Y, Kim H, Moon Y, Kang N (2019) Effect of initial grain size on friction stir weldability for rolled and cast CoCrFeMnNi high-entropy alloys. *Metals and Materials International*
 8. Park S, Park C, Na Y, Kim H-S, Kang N (2019) Effects of (W, Cr) carbide on grain refinement and mechanical properties for CoCrFeMnNi high entropy alloys. *J Alloy Compd* 770:222–228
 9. Richter T, Giese M, Rhode M, Schroepfer D, Michael T, Fritsch T (2021) Influence of surface preparation on cracking phenomena in TIG-welded high and medium entropy alloys. *Journal of Manufacturing and Materials Processing* 6(1)
 10. Nam H, Park S, Chun E-J, Kim H, Na Y, Kang N (2019) Laser dissimilar weldability of cast and rolled CoCrFeMnNi high-entropy alloys for cryogenic applications. *Sci Technol Weld Joining* 25(2):127–134
 11. ISO, ISO/TR 581:2005 Weldability — metallic materials — general principles, 2005
 12. Xu N, Song Q, Bao Y (2019) Microstructure evolution and mechanical properties of friction stir welded FeCrNiCoMn high-entropy alloy. *Mater Sci Technol* 35(5):577–584
 13. Heidarzadeh A, Mironov S, Kaibyshev R, Çam G, Simar A, Gerlich A, Khodabakhshi FF, Mostafaei A, Field DP, Robson JD, Deschamps A, Withers PJ (2021) Friction stir welding/processing of metals and alloys: a comprehensive review on microstructural evolution. *Prog Mater Sci* 117(1):100752
 14. DIN, DIN EN ISO 6520 - 2: Einteilung von geometrischen Unregelmäßigkeiten an Metallen, Pressschweißungen, 2001
 15. Oliveira JP, Shen J, Zeng Z, Park JM, Choi YT, Schell N, Maawad E, Zhou N, Kim HS (2022) Dissimilar laser welding of a CoCrFeMnNi high entropy alloy to 316 stainless steel. *Scr Mater* 206(1):114219
 16. Oliveira JP, Shamsolhodaei A, Shen J, Lopes JG, Gonçalves RM, de Brito Ferraz M, Piçarra L, Zeng Z, Schell N, Zhou N, Kim HS (2022) Improving the ductility in laser welded joints of CoCrFeMnNi high entropy alloy to 316 stainless steel. *Mater Des* 219(1):110717
 17. Samiuddin M, Li J, Muzamil M, Khan S, Xiong J (2022) Parametric optimization of diffusion welding process in joining of CoCrNi medium-entropy alloys (MEA) and SUS 304 Stainless Steel Using Full Factorial Design. *Jom* 74(11):4280–4293
 18. Richter T, Schroepfer D, Rhode M, Boerner A, Neumann RS, Schneider M, Laplanche G (2022) Influence of machining on the surface integrity of high- and medium-entropy alloys. *Mater Chem and Phys* 275(1):125271
 19. Stephan-Scherb C, Schulz W, Schneider M, Karafiludis S, Laplanche G (2021) High-temperature oxidation in dry and humid atmospheres of the equiatomic CrMnFeCoNi and CrCoNi high- and medium-entropy alloys. *Oxid Met* 95(1–2):105–133
 20. Jin K, Sales BC, Stocks GM, Samolyuk GD, Daene M, Weber WJ, Zhang Y, Bei H (2016) Tailoring the physical properties of Ni-based single-phase equiatomic alloys by modifying the chemical complexity. *Sci Rep* 6:20159
 21. Book SMR (2004) Elsevier Butterworth Heinemann. Great Briton, Oxford
 22. Smithells Metals Reference Book, 7 ed., Butterworth-Heinemann, Oxford, England, 1992
 23. Chen BR, Yeh AC, Yeh JW (2016) Effect of one-step recrystallization on the grain boundary evolution of CoCrFeMnNi high entropy alloy and its subsystems. *Sci Rep* 6:22306
 24. Wu Z, David SA, Leonard DN, Feng Z, Bei H (2018) Microstructures and mechanical properties of a welded CoCrFeMnNi high-entropy alloy. *Sci Technol Weld Joining* 23(7):585–595
 25. Yang J, Wu J, Zhang CY, Zhang SD, Yang BJ, Emori W, Wang JQ (2020) Effects of Mn on the electrochemical corrosion and passivation behavior of CoFeNiMnCr high-entropy alloy system in H₂SO₄ solution. *J Alloys Compd* 819(1):152943
 26. Wu Z, Bei H, Otto F, Pharr GM, George EP (2014) Recovery, recrystallization, grain growth and phase stability of a family of FCC-structured multi-component equiatomic solid solution alloys. *Intermetallics* 46:131–140

Publisher's Note Springer Nature remains neutral with regard to jurisdictional claims in published maps and institutional affiliations.

Springer Nature or its licensor (e.g. a society or other partner) holds exclusive rights to this article under a publishing agreement with the author(s) or other rightsholder(s); author self-archiving of the accepted manuscript version of this article is solely governed by the terms of such publishing agreement and applicable law.